Detection of Satellite Maneuvers in Earth and Cislunar Orbits using Adaptive CuSum Methods

Kevin J Franzblau *The Charles Stark Draper Laboratory*
Rami S Mangoubi, *The Charles Stark Draper Laboratory*
Hermann K Sipowa, *True Anomaly, Inc.*

ABSTRACT

The tracking of satellite and resident space object (RSO) trajectories is essential to both space situational awareness and celestial navigation. As such, detection of maneuvers and other orbital anomalies of RSOs constitutes a challenge to be addressed. This work discusses the application of an adaptive automated multiple CuSum algorithm on geocentric and cislunar satellites to detect impulsive maneuvers. Historically both data and model-based approaches have been used to address this problem. These methods rely on the deviation of each data point to some predicted value and rely on parameter tuning. This study leverages and further develops the previous work by introducing a statistical perspective, the CuSum algorithm. It relies on invariant orbital elements for maneuver detection. Real data from both geocentric and cislunar satellites are used to test the methodology. Using Two-Line Elements or TLE data for six Low Earth Orbit RSOs, catch rates of over 96% within a few data points after their occurrence are achievable, with an occurrence of only 1 false alarm per 400 days. For satellites and ephemeris real data from two flown cislunar missions the algorithm achieves catch rates of over 98% and false alarm rates of over 68 days per false alarm. Adjusting the threshold provides a trade off in catch and false alarm rates.

Keywords: Maneuver Detection, Space Situational Awareness, RSO Tracking, CuSum, Cislunar Space, LEO, Orbit Determination, TLE, Statistical, Data-Driven

I. INTRODUCTION

1. Background and Motivation

As the tracking of satellites continue to play essential roles in national security, space situational awareness remains a topic of serious interest for the United States. Consequently, understanding the behavior of resident space objects (RSOs) is essential. Satellites regularly perform maneuvers for reasons such as orbit maintenance, to prevent decay, or strategic maneuvering to change their orbit for a new objective. Change in orbit can be achieved by low thrust engines that gradually adjust the satellite's course or more rapidly by impulsive maneuvers. Being the faster option, impulsive maneuvers are important to recognize and identify in order to adjust predictions of the observed RSO's trajectory across all ranges of geocentric orbits including more stable *geosynchronous orbits* (GEO), *middle Earth orbit* (MEO), as well as *low Earth orbit* (LEO), and *very low Earth orbit* (VLEO). Additionally, the US Space Force has emphasized the importance of space situational awareness beyond the geocentric regime [1]. As further missions are undertaken in *cislunar space*, the need for enhanced space situational awareness continues to grow. Due to the chaotic nature of cislunar space, small maneuvers have large consequences on the orbit of the spacecraft, quick and reliable detections of maneuvers are therefore essential to understanding their behavior.

2. Problem Statement

This study aims to develop the capability to reliably detect the occurrence of impulsive maneuvers undertaken in both Earth orbiting and cislunar satellites. To achieve this objective, two-line element (TLE) state data and maneuver information from both earth orbit satellites in low Earth orbit (LEO), as well as real data for cislunar spacecraft are used to test the efficacy of the developed statistical methods based on the CuSum algorithm.

3. Previous Work

Historically both data and model-based approaches addressed the challenge of satellite maneuver detection. Lemmens and Krag used a dynamics model to compare orbital element measurements to predicted values propagated from the previous observation in their TLE consistency check method as well as their robust TLE time series analysis method that uses historical TLE data for anomaly detection [2]. Kelecy proposed a data-driven approach using adjacent sliding windows over orbital invariant sets. Polynomial fits of a leading and trailing window are used to find extrapolated distance values between the windows to apply a threshold test to [3]. Patera utilized a related approach with one window used to fit a polynomial that is then extrapolated and compared to the next orbital element data point against a threshold [4]. Folcik et al. implemented a binary search algorithm focused on geosynchronous Earth orbits to detect maneuvers, but with limited detection capabilities of smaller maneuvers (on

the order of 0.1-0.01 m/s) [5]. Yang and Pastor proposed the use of nonlinear uncertainty propagation along decussated orbital arc [6]. Porcelli proposed a method using the weighted root mean square of RSO observations in comparison to a predicted post maneuver track. This method compares the distance between a pre-maneuver trajectory and a post maneuver one [7]. Perovich used a few different approaches based on machine learning, both using decision trees and deep learning approaches [8].

4. Approach and Contributions

The CuSum Algorithm. This study leverages and further develops the mentioned work by introducing a statistical perspective, the CuSum algorithm, for maneuver detection [9], [10], [11]. This data-driven algorithm provides the capability to detect maneuvers that are small in comparison to the noise present as well as not being model dependent like many other methods. A data driven algorithm is particularly helpful when the dynamics become harder to predict as in LEO or more significantly in VLEO. It relies on invariant orbital parameters for impulsive maneuver detection. The adapptive CuSum algorithm is an automated adaptive statistical sequential method that simultaneously estimates the noise parameters, such as means and variances in data windows, and recognizes unexpected changes, based on an adaptive data driven threshold. A simulated satellite maneuver is first used to develop a model-based CuSum algorithm for maneuver detection using multiple orbital elements.

Application to TLE LEO data. Semi-major axis data from two-line element datasets (TLEs) of six low Earth orbit satellites are used to test the data-driven algorithm. This data-driven multiple CuSum algorithm used for maneuver detection uses two different CuSum implementations at once to best handle detection due to the inherently unknown nature of the maneuver as well as the presence of both process and measurement noise.

Application to Cislunar orbits. Additionally, this study also introduces a CuSum algorithm design to cislunar maneuver detection. By monitoring the most stable term of a three-body system, the Jacobi constant, a unique data-driven algorithm is used to detect impulsive maneuvers of cislunar spacecraft. Ephemeris data from two cislunar missions (Artemis P1 and P2) are used to test its abilities on recognizing smaller station-keeping maneuvers as well as more impactful orbit transfer maneuvers.

5. Organization

This study will first introduce the approach to the problem by defining necessary orbital parameters and their uses as inputs for maneuver detection methods developed in subsections II.1 and II.2. The base for these methods, the CuSum algorithm, will be introduced along with more specific adaptations appropriate to the application including parameter estimation and adaptive thresholding in II.3 - II.5. The algorithm will then first be demonstrated on simulated satellite data, explaining the specific model-based method developed for this use case when the dynamics are well known in III. The results are shown under different maneuver magnitudes and direction. Next, the algorithm will be applied to real satellite data in the form of TLE datasets and corresponding maneuver logs for six missions in IV. An automated data-driven approach is taken to this data due to infrequent sampling and modeling difficulties with resulting performance metrics. Lastly, in section V, the algorithm will be applied to cislunar spacecraft through an alternate data-driven CuSum-based method with the use of a high-pass filter. This will utilize real ephemeris and maneuver data from two cislunar missions.

II. PROBLEM FORMULATION AND APPROACH

1. Earth Orbiting

Earth Orbit Dynamics. The dynamics of a satellite in orbit under a simplified two body Keplerian systems is governed by the state vector $\vec{X}$ in (1) and corresponding equations of motion $\dot{\vec{X}}$ in (2), with μ_G representing the gravitational parameter of Earth. The vector $\vec{r}$ is the position in Earth Centered Inertial (ECI) coordinates with magnitude r and components r_x, r_y, and r_z, and similarly the velocity $\vec{v}$ is defined as the velocity with magnitude v and components v_x, v_y, and v_z [12].

$$\vec{X} = \begin{bmatrix} r_x \\ r_y \\ r_z \\ \dot{r_x} \\ \dot{r_y} \\ \dot{r_z} \end{bmatrix} = \begin{bmatrix} r_x \\ r_y \\ r_z \\ v_x \\ v_y \\ v_z \end{bmatrix} \tag{1}$$

$$\dot{\vec{X}} = \begin{bmatrix} v_x \\ v_y \\ v_z \\ -\mu_G \frac{x}{r^3} \\ -\mu_G \frac{y}{r^3} \\ -\mu_G \frac{z}{r^3} \end{bmatrix} \tag{2}$$

The Orbit Invariants. With these dynamics, satellite state data consisting of position and velocity components vary across their orbits. However, satellite states can be converted into orbital elements consisting of five stationary terms and one which oscillates. These five terms describe the shape and orientation of the orbit and, under idealized two body Keplerian conditions, are completely invariant. In real life data these terms are not constant but act stable while only varying slowly. These five terms are the *semi-major axis* a, *eccentricity* e, *inclination* i, *longitude of ascending node* Ω, and *argument of periapsis* ω. Their definition can be seen in equations (3) - (9), where $\vec{h}$ and $\vec{n}$ represent the angular momentum and node vectors used to compute the other elements, $\hat{k}$ represents the unit vector in the positive z direction, and $\vec{e}$ is the eccentricity vector whose magnitude is the eccentricity quantity that is useful as an orbital invariant.

$$\vec{h} = \vec{r} \times \vec{v} \tag{3}$$

$$\vec{n} = \hat{k} \times \vec{h} \tag{4}$$

$$\vec{e} = \frac{(v^2 - \frac{\mu_G}{r})\vec{r} - (\vec{r} \cdot \vec{v})\vec{v}}{\mu} \tag{5}$$

$$a = \frac{h^2}{\mu_G(1 - e^2)} \tag{6}$$

$$i = cos^{-1}(\frac{h_z}{h}) \tag{7}$$

$$\Omega = cos^{-1}(\frac{n_x}{n}) \tag{8}$$

$$\omega = cos^{-1}(\frac{\vec{e} \cdot \vec{n}}{en}) \tag{9}$$

The invariant nature of these terms makes them ideal for monitoring for maneuver occurrences. These terms should remain constant, or relatively stable under more realistic conditions, until a maneuver occurrence causing them to jump. TLE datasets used to validate the methods efficacy on real satellites provide these invariants for real life RSOs. The effect of maneuvers on these elements is determined by both magnitude and direction of the maneuver. For instance, In-plane maneuvers that occur when a satellite undergoes a change in velocity within its orbital plane exhibit changes in terms such as semi-major axis a and eccentricity e. Conversely, out-of-plane maneuvers, that occur when a satellite experiences a change in velocity tangential to its orbital plane, affect the satellite's inclination i.

2. Cislunar Orbiting

Three Bodies: Earth, Moon, and Spacecraft Dynamics. The three-body environment introduces the major effect of the gravitational pull of the moon onto the dynamics of the satellite. These new dynamics when assuming a simplified circular restricted three body (CR3BP) system is shown by the state vector $\vec{X}$ in (10) and corresponding equations of motion $\dot{\vec{X}}$ in (11). Where $x_s, y_s, z_s, \dot{x}_s, \dot{y}_s$, and $\dot{z}_s$ represent the state of the spacecraft in the Earth-Moon synodic frame centered at the barycenter of the two bodies. The term $r_{E/S}$ represents the distance between the spacecraft and Earth, $r_{M/S}$ represents the distance between the spacecraft and the Moon, $r_{B/E}$ represents the distance between the Earth and the barycenter, and $r_{B/M}$ represents the distance between the Moon and the barycenter. The gravitational parameter for the Earth and Moon are defined as μ_G and μ_M, and ω_s is the angular rate of the rotating synodic frame which is equivalent to the angular speed of the Moon [12].

$$\vec{X} = \begin{bmatrix} x_s \\ y_s \\ z_s \\ \dot{x_s} \\ \dot{y_s} \\ \dot{z_s} \end{bmatrix} \tag{10}$$

$$\dot{\vec{X}} = \begin{bmatrix} \dot{x}_s \\ \dot{y}_s \\ \dot{z}_s \\ \frac{-\mu_G(x_s+r_{B/E})}{r^3_{E/S}} - \frac{\mu_M(x_s-r_{B/M})}{r^3_{M/S}} + 2\omega_s\dot{y}_s + \omega_s^2 x_s \\ \frac{-\mu_G y_s}{r^3_{E/S}} - \frac{\mu_M y_s}{r^3_{M/S}} - 2\omega_s\dot{x}_s + \omega_s^2 y_s \\ \frac{-\mu_G z_s}{r^3_{E/S}} - \frac{\mu_M z_s}{r^3_{M/S}} \end{bmatrix} \tag{11}$$

The Jacobi Constant. Because of the impact of the Moon's gravity, the same stable orbital elements in Earth orbiting satellites, are not invariant in the cislunar regime. However, the *Jacobi constant* is a parameter that serves as a reliable cislunar orbital invariant. This is a term that relates to orbital energy through a pseudo potential term U^*, shown in equation (12), and a velocity related term K^*, shown in equation (13), and is defined as J in equation (14) [12].

$$U^* = \frac{2\mu_G}{r_{E/S}} + \frac{2\mu_M}{r_{M/S}} + \omega_s^2(x_s^2 + y_s^2) \tag{12}$$

$$K^* = \dot{x}_s^2 + \dot{y}_s^2 + \dot{z}_s^2 \tag{13}$$

$$J = U^* - K^* \tag{14}$$

Under idealized circular restricted three body assumptions, the Jacobi constant is the only conserved quantity and therefore the most reliable term available to be monitored for maneuvers. Similarly to the invariants in earth orbit satellites, this term should remain constant until the occurrence of a maneuver.

3. CuSum Introduction and Overview

The CuSum algorithm is a sequential analysis technique that aims to detect parameter changes in noisy data. It can recognize slight and persistent changes in a signal through the accumulation of deviation from an initial distribution. It achieves this objective through the use of a likelihood ratio test between the predicted probability density functions of a null hypothesis and a change or jump hypothesis, which is continuously summed over a series [13], [14]. This study will demonstrate the use of three types of Cusum for detection of change in mean, variance, and both parameters simultaneously.

Cusum for Change in Mean. The mean change CuSum assumes that any change point in the signal will have no effect on its variance but strictly affects the mean. The step-by-step process of the algorithm can be seen as follows:

- *The Hypothesis Test.* The algorithm begins with the definition of two hypotheses, the null and jump. Both of these hypotheses assume a Gaussian distribution of the input signal, x, with known signal mean, μ, and known standard deviation, σ. The null hypothesis, H_0, assumes a mean μ_0 and a standard deviation, σ and the jump hypothesis, H_1, assumes a mean μ_1 and the same standard deviation, σ, as shown in (16) and(15).

$$H_0 : \mu = \mu_0, \sigma = \sigma \tag{15}$$

$$H_1 : \mu = \mu_1, \sigma = \sigma \tag{16}$$

- *The underlying Probability Model.* The probability density functions are then computed for both hypotheses at time index n by, in this study, using the Gaussian distributions, (17), with input σ and μ from the hypothesis definitions.

$$p\left(n, \mu, \sigma\right) = \frac{1}{\sigma\sqrt{2\pi}} e^{\frac{-(x(n)-\mu)^2}{2\sigma^2}} \tag{17}$$

- *The Likelihood Ratio.* The log likelihood ratio test, L, is then taken at position n in the series between the probability density functions of the jump and null hypotheses in (18).

$$L\left(n\right) = \ln \frac{p\left(n, \mu_1, \sigma\right)}{p\left(n, \mu_0, \sigma\right)} \tag{18}$$

- *Specializing the Likelihood Ration to the Mean.*After substituting (17) into (18) L can be simplified into the following in (19). Because the signal value at point n is more likely to be from the null hypothesis than the jump hypothesis before the change point, L tends to be negative before this point and because the opposite is true after the change point, L tends to be positive after it.

$$L\left(n\right) = \frac{\mu_1 - \mu_0}{2\sigma^2}(2x(n) - \mu_1 - \mu_0) \tag{19}$$

- *Summing the Log Likelihood Ratio over Intervals.* The likelihood ratios of the entire series up until time index n are then summed, S, in (20). This summation allows for the accumulation of the signal's deviation from the null hypothesis to the jump once the change point occurs.

$$S\left(n\right) = \sum_{k=1}^{n} L(k) \tag{20}$$

  The ratios L in (19) are substituted into (20) to produce S in (21). Because L is typically negative before the change point and positive after, S will tend to trend downwards until this point and upwards after.

$$S\left(n\right) = \sum_{k=1}^{n} \frac{\mu_1 - \mu_0}{2\sigma^2}(2x(k) - \mu_1 - \mu_0) \tag{21}$$

- *The Indicator Function.* To eliminate this initial negative trend to generate a series stable until the change point, the indicator function, h, is found at n by subtracting the minimum value of the series S from entry 1 to entry n-1 from S in (22). This creates a term which remains steady until the change point event occurrence at which point it will continuously rise.

$$h\left(n\right) = S\left(n\right) - min_{1<k<n-1}(S(k)) \tag{22}$$

- *Threshold Comparison.* Finally a threshold test, τ, is applied to the indicator h to detect a change point at position n_c when the condition in (23) is first met.

$$h\left(n_c\right) \geq \tau \tag{23}$$

  The threshold is adaptive, and may vary over time, and the adaptation is described below in Section II.4 and II.5.

An example mean change signal $x(n)$ and resulting $L(n)$, $S(n)$, and $h(n)$, when passed through this CuSum can be seen in Figure 1.

Cusum for Change in Variance. Conversely, the variance change CuSum case is able to take a noisy input signal and recognize when a change in signal variance has occurred. The variance change CuSum assumes that any change point in the signal will have no effect on its mean but strictly affects the variance. The step-by-step process of the algorithm can be seen as follows:

- The algorithm still begins with a null and jump hypothesis of known parameters, H_0 and H_1, but the means are assumed to be constant across both hypotheses in this case, with unique variances, which can be seen in (25) and (24).

$$H_0 : \mu = \mu, \sigma = \sigma_0 \tag{24}$$

$$H_1 : \mu = \mu, \sigma = \sigma_1 \tag{25}$$

- The log likelihood ratio test, L, is then taken between the two distributions defined in (25) and (24) to produce (26).

$$L\left(n\right) = \ln \frac{\sigma_0}{\sigma_1} + \frac{(x(k) - \mu)^2(\sigma_1^2 - \sigma_0^2)}{2\sigma_0^2\sigma_1^2} \tag{26}$$

- L in (26) is substituted into (20) to produce S in (27).

$$S\left(n\right) = \sum_{k=1}^{n} \ln \frac{\sigma_0}{\sigma_1} + \frac{(x(k) - \mu)^2(\sigma_1^2 - \sigma_0^2)}{2\sigma_0^2\sigma_1^2} \tag{27}$$

- Lastly, S in (27) is substituted into (22) to generate the indicator h and a threshold test is applied on this using (23).

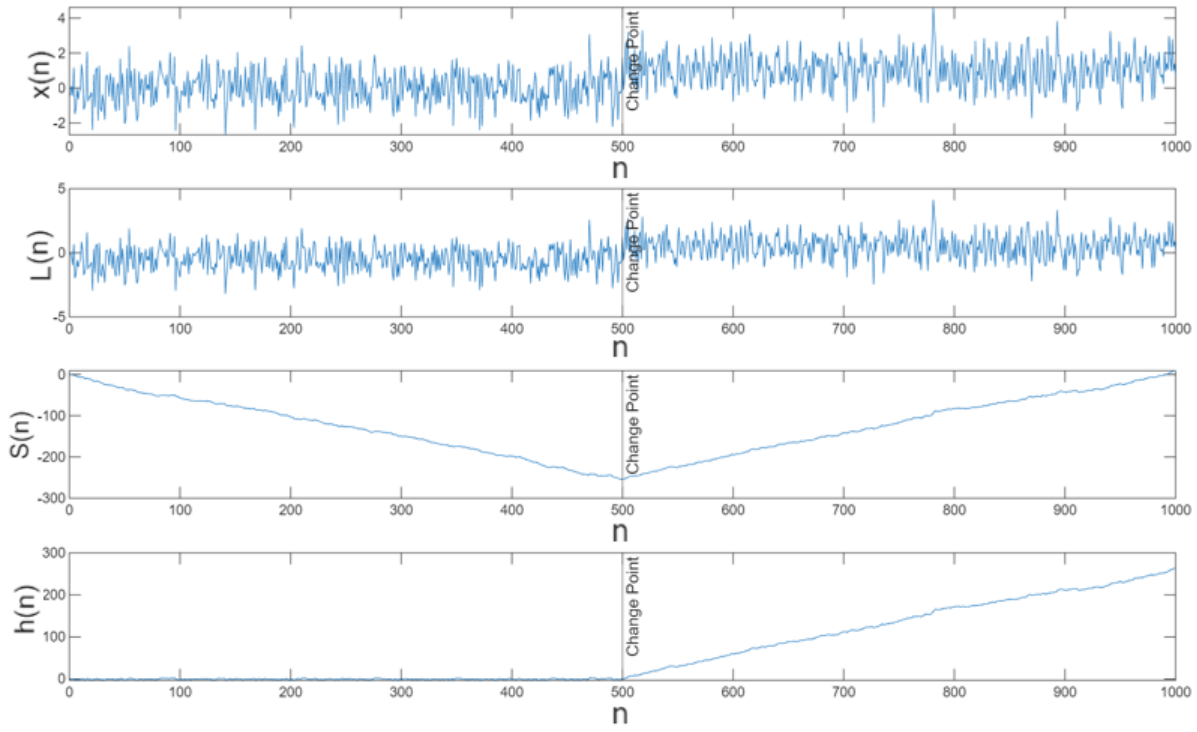

Figure 1: Behavior of mean change CuSum on example signal, with input signal (top) and final indicator function continuously rising after change point occurrence (bottom).

CuSum for Change in both Mean and Variance. The mean and variance change CuSum case is able to take a noisy input signal and recognize when a change in signal mean or variance has occurred. This case assumes neither the mean nor the variance remains constant across a change point. The step-by-step process of the algorithm is:

- The algorithm still begins with a null and jump hypothesis, H_0 and H_1, but the known means and variances for both are assumed to be unique, which can be seen in (29) and (28).

$$H_0 : \mu = \mu_0, \sigma = \sigma_0 \tag{28}$$

$$H_1 : \mu = \mu_1, \sigma = \sigma_1 \tag{29}$$

- The log likelihood ratio test, L, is then taken between the two distributions defined in (29) and (28) to produce (30).

$$L\left(n\right) = \ln \frac{\sigma_0}{\sigma_1} + \frac{(x(n) - \mu_0)^2\sigma_1^2 - (x(n) - \mu_1)^2\sigma_0^2}{2\sigma_0^2\sigma_1^2} \tag{30}$$

- L in (30) is substituted into (20) to produce S in (31).

$$S\left(n\right) = \sum_{k=1}^{n} \ln \frac{\sigma_0}{\sigma_1} + \frac{(x(k) - \mu_0)^2\sigma_1^2 - (x(k) - \mu_1)^2\sigma_0^2}{2\sigma_0^2\sigma_1^2} \tag{31}$$

- Lastly, S in (31) is substituted into (22) to generate the indicator h and a threshold test is applied on this using (23)

4. Parameter Estimation and the Adaptive CuSum Algorithm

So far, the parameters for the distributions of each hypothesis have been treated as known constants. Often, these parameters are unknown and not entirely constant, invoking the need for their estimation. The specific estimation approaches of these means

and variances for the null and change hypotheses are specific to the adaptation of CuSum applied to each use case in this study and will be discussed in further detail in their respective sections. However, they all rely on sliding window approximations. As the CuSum is applied along the signal at index n, the mean $\hat{\mu}$ and variance $\hat{\sigma}^2$ can be estimated locally by the use of a window of previous data of size N, shown in (32) and (33).

$$\hat{\mu}(n) = \frac{\sum_{i=n-N}^{n} x(i)}{N} \tag{32}$$

$$\hat{\sigma}(n)^2 = \frac{1}{N-1} \sum_{i=n-N}^{n} \left(x\left(i\right) - \hat{\mu}(n)\right)^2 \tag{33}$$

The localized parameter estimation being utilized in this study gives resilience to gradual changes in the data not caused by impulsive maneuver occurrences. The use of this estimation to form the time varying distributions for the algorithm creates the Adaptive CuSum algorithm.

5. Adaptive Thresholding

This selection of the threshold, τ, is a nontrivial process that involves a tradeoff between multiple performance metrics such as detection speed, detection catch rate, and false alarm rate. The indicator function does not remain perfectly constant before the maneuver occurrence and experiences variability due to noise in the input signal and off-Keplerian and off-CR3BP behavior. A threshold set too low will cause false alarms, while one too high will take longer for detection to occur. To allow for quick and reliable detection across different noise and maneuver magnitudes, an adaptive threshold is developed.

The threshold used in this study is made adaptive through the use of sliding window of size N estimations of the median and mean absolute deviation of the indicator function. The mean absolute deviation, MAD_h, estimate is shown in (34), where $\hat{\mu}_h$ is the local mean of the indicator found using (32), with the indicator h being used as the input signal x in the equation. This adaptive threshold, τ, is set as a multiple, k, of the estimated local mean absolute deviations, MAD_h, of the indicator above its estimated local median, M_h, of the window in (35).

$$MAD_h(n) = \frac{\sum_{i=n-N}^{n} |h(i) - \hat{\mu}_h(n)|}{N} \tag{34}$$

$$\tau = M_h(n) + k * MAD_h(n) \tag{35}$$

This serves to provide a more robust threshold that can reliably detect the change point in the signal data under different properties of the data where k serves as a tunable value depending on the desired focus on minimal false alarms vs fast detection speeds.

III. MODEL-DRIVEN APPROACH ON SIMULATED DATA

1. Simulation

To verify the efficacy of the algorithm in maneuver detection, simulated data is used initially. A simulation is developed with the occurrence of a singular impulsive maneuver of varying directions and magnitudes and operating at a sample rate of ten hertz. The simulation generates state data for the satellite with both measurement and process noise present. It uses the dynamics model provided in the High Precision Orbit Propagator(HPOP) implemented by Mahooti [15]. This method includes a spherical harmonics gravity model of the Earth representing the non-uniform mass distribution due to the Earth's oblateness and surface irregularities. In addition to the effects of Earth's gravity other perturbing forces are modeled including point mass representations of other celestial bodies (such as the Moon, Sun, and other planets), solar radiation pressure, atmospheric drag, general relativity, and both solid Earth and ocean tides. The state space representation of this system can be seen as follows.

The state vector $\vec{X}$ and state derivative vector $\dot{\vec{X}}$ are defined in equations (36) and (37) where the vectors $\vec{r}$ and $\vec{v}$ represent the position and velocity of the satellite in ECI coordinates. The vector $\vec{a}$ represents the acceleration that the satellite experiences due to the modeled dynamics. The vector $\vec{u}$ represents the modeled impulsive maneuver and mapping matrix $\mathbf{B}$ maps the effect of this thrust onto the dynamics. The vector $\vec{w}$ represents the process noise representative of unmodeled dynamic effects with the corresponding matrix Γ mapping this process noise onto the state derivative.

$$\vec{X}(t) = \begin{bmatrix} \vec{r}(t) \\ \vec{v}(t) \end{bmatrix} \tag{36}$$

$$\dot{\vec{X}}(t) = \begin{bmatrix} \vec{v}(t) \\ \vec{a}(t) \end{bmatrix} + \mathbf{B}\vec{u}(t) + \mathbf{\Gamma}\vec{w}(t) \tag{37}$$

The breakdown of the dynamics components included can be seen in (38) where the acceleration $\vec{a}$ can be broken into the acceleration effects caused by the spherical harmonic model $\vec{a}_{harmonics}$, the Earth and ocean tides $\vec{a}_{tides}$, atmospheric drag $\vec{a}_{drag}$, solar radiation pressure $\vec{a}_{radiation}$, general relativity $\vec{a}_{relativity}$, the Moon $\vec{a}_{Moon}$, the Sun $\vec{a}_{Sun}$, and all other planets in the solar system $\vec{a}_{planets}$.

$$\vec{a}(t) = \vec{a}_{harmonics}(t) + \vec{a}_{tides}(t) + \vec{a}_{drag}(t) + \vec{a}_{radiation}(t) + \vec{a}_{relativity}(t) + \vec{a}_{Moon}(t) + \vec{a}_{Sun}(t) + \vec{a}_{planets}(t) \tag{38}$$

The maneuver $\vec{u}$ is a 3×1 vector with nonzero constant components u_x, u_y, and u_z during the short thrust period between the maneuver start time t_{start} and concluding time t_{end} and is a zero vector $\vec{0}_{3\times1}$ when the thrust is not occurring. This conditional relationship can be seen in (39). The matrix $\mathbf{B}$ maps the maneuver vector onto the dynamics in (40), where $\mathbf{0}_{3\times3}$ is a 3×3 zero matrix and $\mathbf{I}_{3\times3}$ is a 3×3 identity matrix. The simulation used a short maneuver duration of 10 seconds to emulate an impulsive thrust and varied the thrust vector direction and magnitude for different trials.

$$\vec{u}(t) = \begin{cases} \begin{bmatrix} u_x \\ u_y \\ u_z \end{bmatrix} & : t_{start} < t < t_{end} \\ \vec{0}_{3\times1} & : otherwise \end{cases} \tag{39}$$

$$\mathbf{B} = \begin{bmatrix} \mathbf{0}_{3\times3} \\ \mathbf{I}_{3\times3} \end{bmatrix} \tag{40}$$

The process noise $\vec{w}$ is a 3×1 vector that samples a normal distribution $\mathcal{N}$ with a mean of zero and variance ${\sigma_{process}}^2$ as shown in (41). This is noise that acts on the acceleration and is mapped onto this using the matrix $\mathbf{\Gamma}$ defined in (42).

$$\vec{w}(t) \sim \mathcal{N}(0, {\sigma_{process}}^2) \tag{41}$$

$$\mathbf{\Gamma} = \begin{bmatrix} \mathbf{0}_{3\times3} \\ \mathbf{I}_{3\times3} \end{bmatrix} \tag{42}$$

The measurement matrix $\vec{Y}$ consists of the state vector $\vec{X}$ with added measurement noise. The 3×1 vector $\vec{\epsilon}_{position}$ represents the noise present on the position data and is filled with random variables sampled from a normal distribution with zero mean and variance ${\sigma_{position}}^2$. The 3×1 vector $\vec{\epsilon}_{velocity}$ represents the noise present on the velocity data and is filled with random variables sampled from a normal distribution with zero mean and variance ${\sigma_{velocity}}^2$. This can be seen in equations (43) - (45).

$$\vec{Y}(t) = \vec{X}(t) + \begin{bmatrix} \vec{\epsilon}_{position}(t) \\ \vec{\epsilon}_{velocity}(t) \end{bmatrix} \tag{43}$$

$$\vec{\epsilon}_{position}(t) \sim \mathcal{N}(0, {\sigma_{position}}^2) \tag{44}$$

$$\vec{\epsilon}_{velocity}(t) \sim \mathcal{N}(0, {\sigma_{velocity}}^2) \tag{45}$$

2. CuSum Adaptation and Implementation for Simulated Data

To detect the maneuver a model-based CuSum algorithm is developed under the assumption of well understood dynamics. First, the state data is transformed into orbital element data, and the initial state propagates forward in time to generate predicted orbital element data. This propagation relies on the accuracy of the modeled dynamics, with greater unmodeled perturbations or process noise invoking the need for frequent resets of the propagator. The predicted states $\hat{\vec{X}}$ are found by using the first measurement $\vec{Y}$ at initial time t_0 as the initial state vector for the integration of the derivative state vector $\dot{\vec{X}}$ defined in (37). State data is then transformed into invariant orbital elements using the vector function $\vec{f}_{oe}(\vec{X})$ representative of the transformation

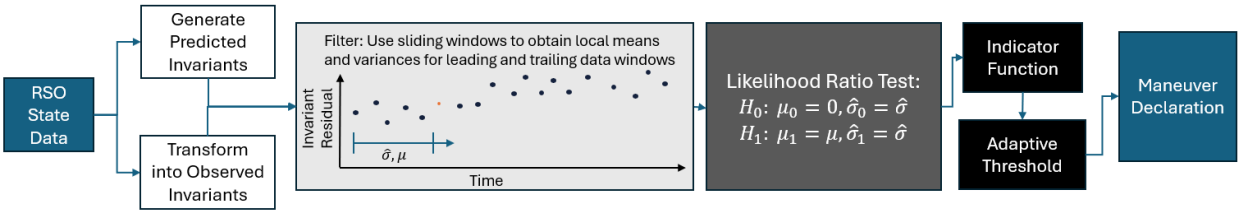

Figure 2: Algorithm architecture for maneuver detection in simulation.

equations (3) - (9). The result of this transformation is an orbital element vector comprised of the semi major axis a, eccentricity e, inclination i, longitude of ascending node Ω, and argument of periapsis ω.

$$\vec{X}_{oe} = \vec{f}_{oe}(\vec{X}) = \begin{bmatrix} a \\ e \\ i \\ \Omega \\ \omega \end{bmatrix} \tag{46}$$

The difference between these observed invariants from output vector $\vec{Y}$ composed of noisy state data and from the predicted state values $\hat{\vec{X}}$ is then computed to form an invariant residual vector $\delta\vec{X}_{oe}$ for each time t in (47).

$$\delta\vec{X}_{oe}(t) = \vec{f}_{oe}(\vec{Y}(t)) - \vec{f}_{oe}(\hat{\vec{X}}(t)) \tag{47}$$

To model the distribution of the residuals, the local mean can be estimated from a trailing sliding window as well as the variance using equation (33), where $\hat{\sigma}$ and $\hat{\mu}$ represent the standard deviation and mean of the chosen invariant residual x and mean of the trailing window with size N. The invariant residual x is a single component of the orbital element residual vector $\delta\vec{X}_{oe}$.

These estimates can then be used to generate the null and maneuver hypotheses. The residual is assumed to be zero-mean in the case of no maneuver and the mean of the trailing window $\hat{\mu}$ in the case of a maneuver occurrence, with the local variance being assumed for both hypotheses. The hypotheses can be seen in equations (48) and (49).

$$H_0 : \mu = 0, \sigma = \hat{\sigma} \tag{48}$$

$$H_1 : \mu = \hat{\mu}, \sigma = \hat{\sigma} \tag{49}$$

These 2 hypotheses are then used implemented in the CuSum algorithm described in equations (17) - (20) to produce S at time t in (50).

$$S\,(n) = \sum_{k=1}^{n} \frac{\hat{\mu}}{2\hat{\sigma}^2}(2x(k) - \hat{\mu}) \tag{50}$$

This summation term S is then used in equation (22) to produce the indicator function h. This indicator can then have an adaptive threshold applied as described in equations (34) and (35). The entire algorithm process can be seen in Figure 2.

3. Performance for Simulated Data

For a simulated maneuver the resulting indicator function and adaptive threshold can be seen in Figure 3. The adaptive threshold reacts to the local variability of the indicator function to limit false alarms and can be applied reliably across different maneuvers and observational noise magnitudes. This prevents the need for tuning to specific scenario properties that a constant value threshold would require.

Effect of Maneuver Magnitude. The resulting detection speed and false alarm rate are both dependent on the threshold selection. Lower thresholds result in faster detection while causing more false alarms. By varying the sensitivity of the adaptive threshold, receiver operator characteristic curves (ROCs) are generated showing the achievable performance and tradeoff between false

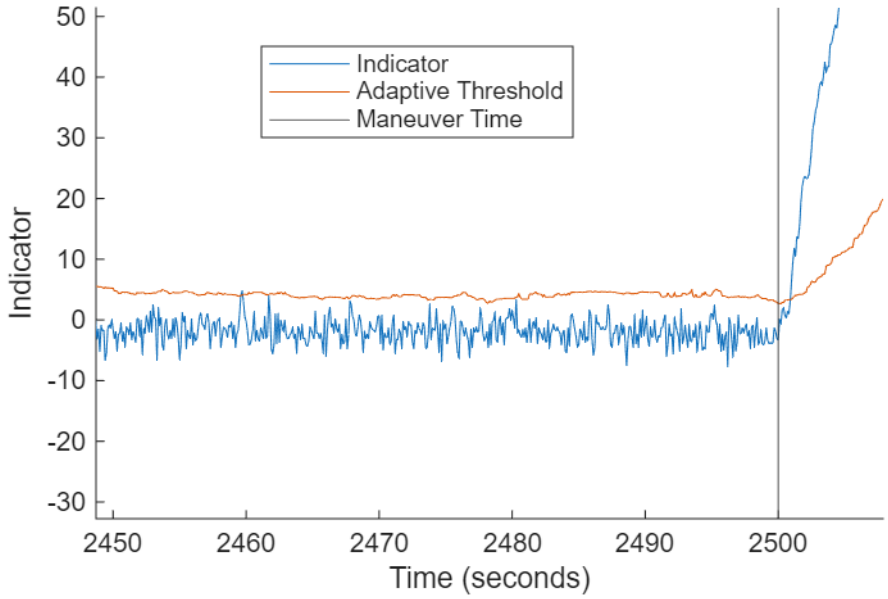

Figure 3: Indicator function and adaptive threshold for detection on simulated data.

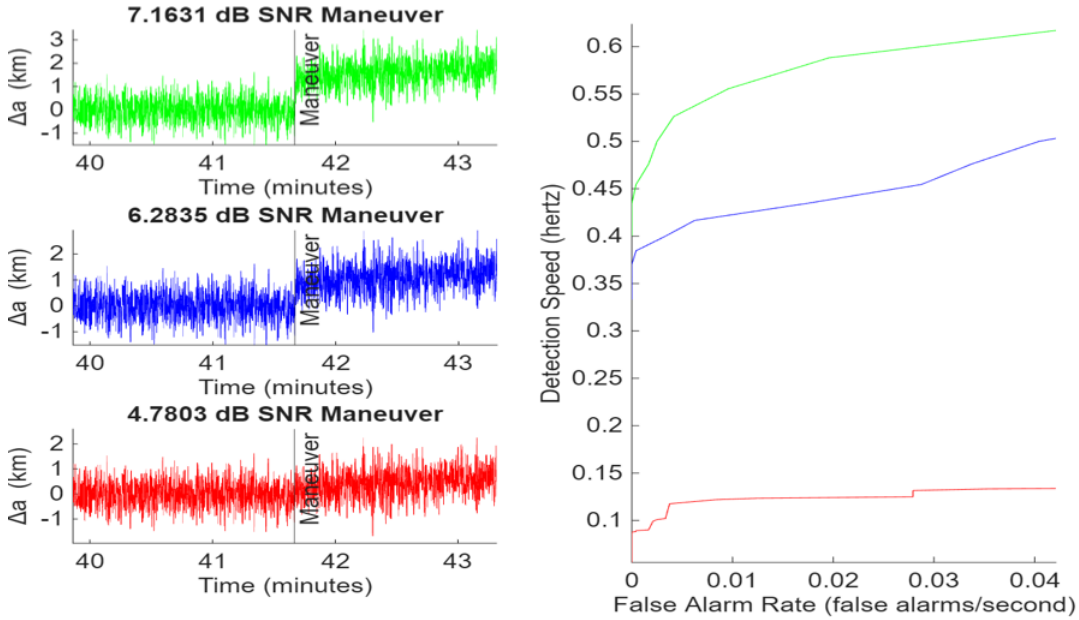

Figure 4: Impact of three maneuvers of varying sizes on semi major axis residual (left) and corresponding ROC performance comparing detection speed and false alarm rate (right).

alarm rate and detection speed. For three simulated in-plane maneuvers the semi major axis residual and corresponding ROC can be seen in Figure 4. The receiver operating characteristic curve shows, by varying the threshold, what detection speed can be produced with its corresponding false alarm rate for the simulated maneuvers.

Choice of Invariant. As previously discussed, the maneuver direction can result in different effects on each invariant. Because of this, a single invariant is not ideal for detection of all types of maneuvers. This motivates the need for the monitoring of multiple invariants for fast detection across all maneuver profiles. This can be seen in Figure 5 where two maneuvers in different directions can be shown impacting both inclination and semi major axis. To achieve optimal performance across all maneuver types, multiple elements are monitored to guarantee the algorithms application on the highest SNR data available.

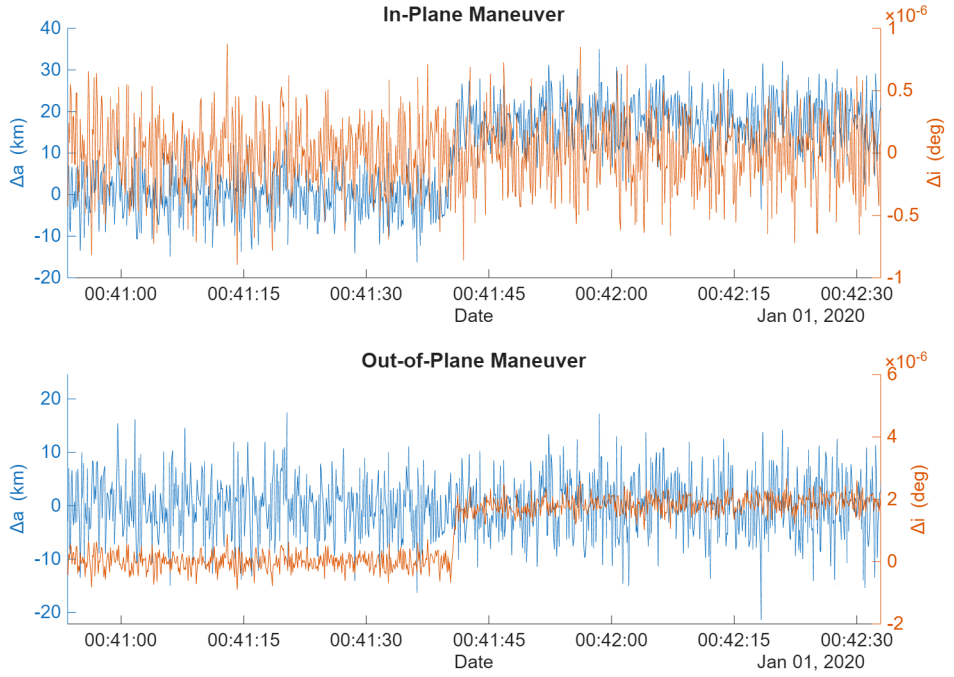

Figure 5: Impact of semi major axis (blue) and inclination (orange) residuals from in-plane maneuver (top) and out-of-plane maneuver (bottom). The first maneuver is in-plane and therefore the semi major axis is affected while inclination is not, and the second maneuver is out-of-plane at the ascending node meaning only the inclination is impacted.

It is to note that the purpose of this section is to get insight into the tradeoff between false alarm rate and time to detection for the CuSum algorithm, for different signal to noise ratios, as indicated by the ROC curves in Figure 4. For that truth values were needed. In general, however, if a model is available and accurate the residual from a Kalman filter based on that model would generate a white residual that would be the basis of a maneuver detection algorithm, by implementing what is known as Fault Detection and Identification methods [16], [17] with the failures representing maneuver in this case. Even in the case where the models contained bounded uncertainties, game theoretical filters can generate signal estimates that are insensitive to these bounded modelling errors while sensitive to the maneuvers, as in [18], [19]).

IV. DATA-DRIVEN APPROACH ON REAL LIFE TLE DATA

1. TLE Data and Associated Challenges

Two-line element sets or TLEs provide orbital element data for six resident space objects [20] and maneuver times are provided by the NASA DORIS service of the same six satellites [21]. The algorithm's detections are compared to the logged maneuver times to evaluate its performance, assumed to be the truth.

The TLE was sampled at an average rate of 2.72 observations per day. The total duration of all six observed missions is over 18474 days. There are 412 logged maneuvers observed with a median ΔV magnitude of 1.93 cm/s. The full distribution of maneuver ΔV magnitudes can be seen in Figure 6.

The application of the same algorithm used on simulated data proved ineffective when used on the TLE data. Low sample rates along with imperfectly modeled dynamics make application of the propagator ineffective. Error between the predicted and observed orbital elements grows rapidly in between the infrequently sampled data. In order to leverage the capability of the CuSum algorithm to $automatically$ detect persistent changes in data, the propagator would have to produce little error when used for many successive data points. Additionally, the properties of the orbital element data is not consistent, often varying in quality significantly between RSOs. This can be seen in Figure 7 where one segment from the RSO Envisat of has minimal noise and apart from maneuver effects, while the other from the RSO Saral has more noise and weaker maneuver effects on the signal. The combination of poorly understood dynamics and low sample rates inspires the need for a data-driven approach to the maneuver detection problem that can detect reliably and automatically in the imperfect TLE dataset. An alternate application of the CuSum is developed to be applicable to this real dataset in order for the implementation to be autonomous in real time.

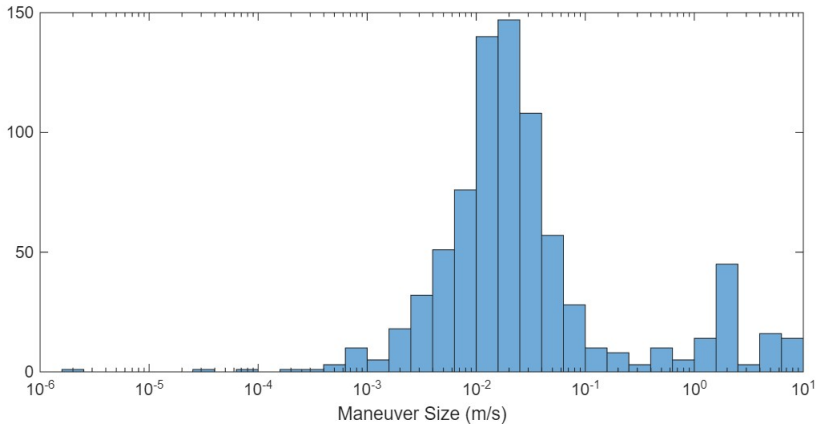

Figure 6: Maneuver ΔV magnitude distribution.

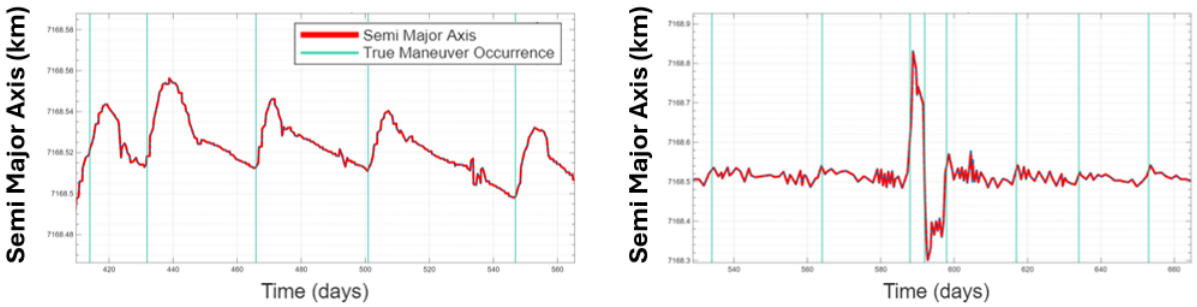

Figure 7: TLE data segment with significant maneuver impact (left) and segment with less apparent impact (right) from two different RSOs. The maneuver occurrences are shown by the vertical green lines.

2. CuSum Adaptation and Implementation

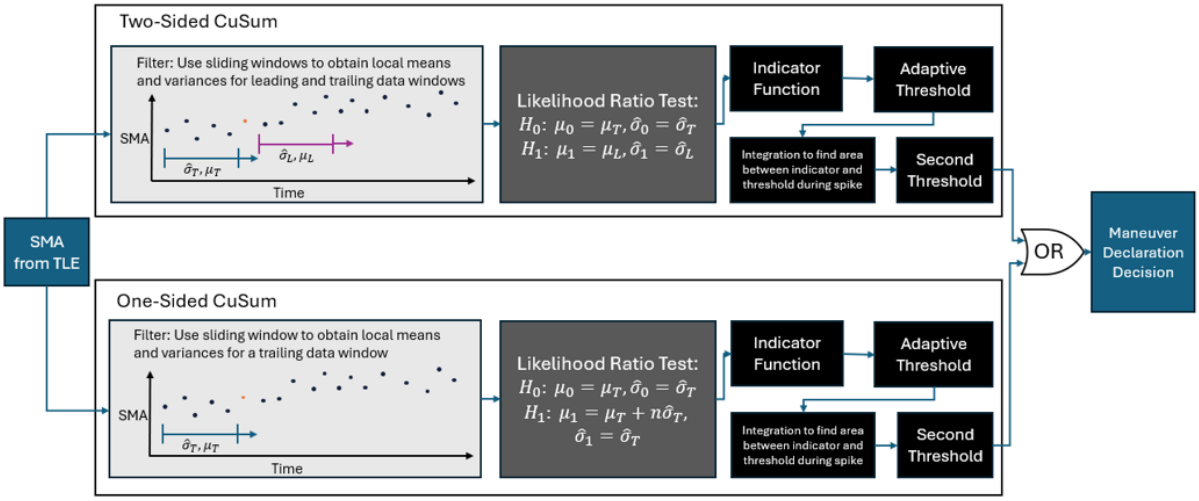

Figure 8: TLE maneuver detection algorithm architecture.

For this study, orbital element data of the semi-major axis, a, is chosen as the signal to be monitored due to its mostly invariant

nature being ideal for CuSum which typically relies on a stationary mean signal. However, due to the non-Keplerian dynamics present, the orbital elements drift with time alongside measurement noise. The semi-major axis proved to be the most stable orbital element. Additionally, due to inaccuracies in maneuver direction and dynamical perturbations present, even maneuvers intended to be strictly out-of-plane have a notable impact on the semi-major axis making this element capable of detecting all types of maneuvers in this dataset. As a result of this drift, along with the tendency for noise variance to change over time, the adaptive CuSum algorithm was developed that continuously estimates the parameters of the signal. It achieves this through the use of a sliding trailing window of data to estimate the local mean and variance that is used for the null hypothesis probability density function estimate. The mean and variance estimate, μ_T and σ_T, can be found using equations (32) and (33). This produces the resulting null hypothesis, H_0, in (51).

$$H_0 : \mu = \mu_T, \sigma = \sigma_T \tag{51}$$

Two separate CuSum-based methods, the two-sided CuSum and the one-sided CuSum, are then applied with unique maneuver hypotheses, as illustrated in Figure 8. The two-sided CuSum utilizes a leading window to estimate the parameters, μ_L and σ_L for local mean and variance, of the jump hypothesis, H_{2S} in the same manner as the trailing window is used for the null hypothesis found using equations (32) and (33). This CuSum is better at detecting maneuvers that are less impulsive and create a more gradual effect on the orbital element data.

$$H_{2S} : \mu = \mu_L, \sigma = \sigma_L \tag{52}$$

The 2 hypotheses defined in (51) and (52) then motivate the CuSum algorithm described in equations (17) - (20) to produce S_{2S} in (53). This summation term S of equation (22) produces the first indicator function h.

$$S_{2S}\left(n\right) = \sum_{k=1}^{n} \ln \frac{\sigma_T}{\sigma_L} + \frac{(x(k) - \mu_T)^2\sigma_L^2 - (x(k) - \mu_L)^2\sigma_T^2}{2\sigma_T^2\sigma_L^2} \tag{53}$$

The one-sided CuSum uses the same variance for both hypotheses with a predicted jump in mean of a multiple of the standard deviation, α, for the jump hypothesis, in (54). This CuSum is the more effective one at recognizing small and more impulsive changes in orbital element data under greater variance.

$$H_{1S} : \mu = \mu_T + \alpha * \sigma_T, \sigma = \sigma_T \tag{54}$$

Like in the case of the first jump hypothesis, the 2 hypotheses defined in (51) and (54) are then used in the CuSum algorithm described in equations (17) - (20) to produce S_{1S} in (55). This summation term S of equation (22) produces the second indicator function h.

$$S_{1S}\left(n\right) = \sum_{k=1}^{n} \frac{\alpha * \sigma_T}{2\sigma_T^2}(2x(k) - 2\mu_T - \alpha * \sigma_T) \tag{55}$$

The resulting two indicator functions both have threshold tests applied to determine when a flag will occur.

3. Adaptive and Automatic Thresholding

An extension to the thresholding method previously discussed is used on this dataset to improve results. In the data-driven application of the CuSum there are many spikes in the indicator that form when the sliding windows pass over a maneuver. A first threshold serves to isolate each spike. This threshold is found using the same process described previously using equations (34) and (35) on both indicators. When the indicator function then rises above this first assigned threshold, it is graphically integrated to find the area between the indicator and the threshold. The area between the indicator function during a spike and the initial threshold is then used for a final, constant threshold test to trigger a maneuver flag. The purpose of this is to filter out anomalies which cause unsustained effects on the semi major axis data that is not indicative of a maneuver occurrence. This integration method weights the duration of the spike in addition to its magnitude, emphasizing sustained changes in the signal. This can be seen in Figure 9 where small, unsustained anomalies cause momentary rises in the initial indicator. However, because they are brief this additional step allows for the greater prominence of the true maneuver occurrence in the final indicator.

The algorithm's application on two pieces of the data set to generate the final indicator is visible in Figure 10. The algorithm is demonstrated to detect maneuvers when applied on higher quality data with larger maneuver effects and poor-quality data with weaker maneuver impact on the semi major axis data relative to its noise.

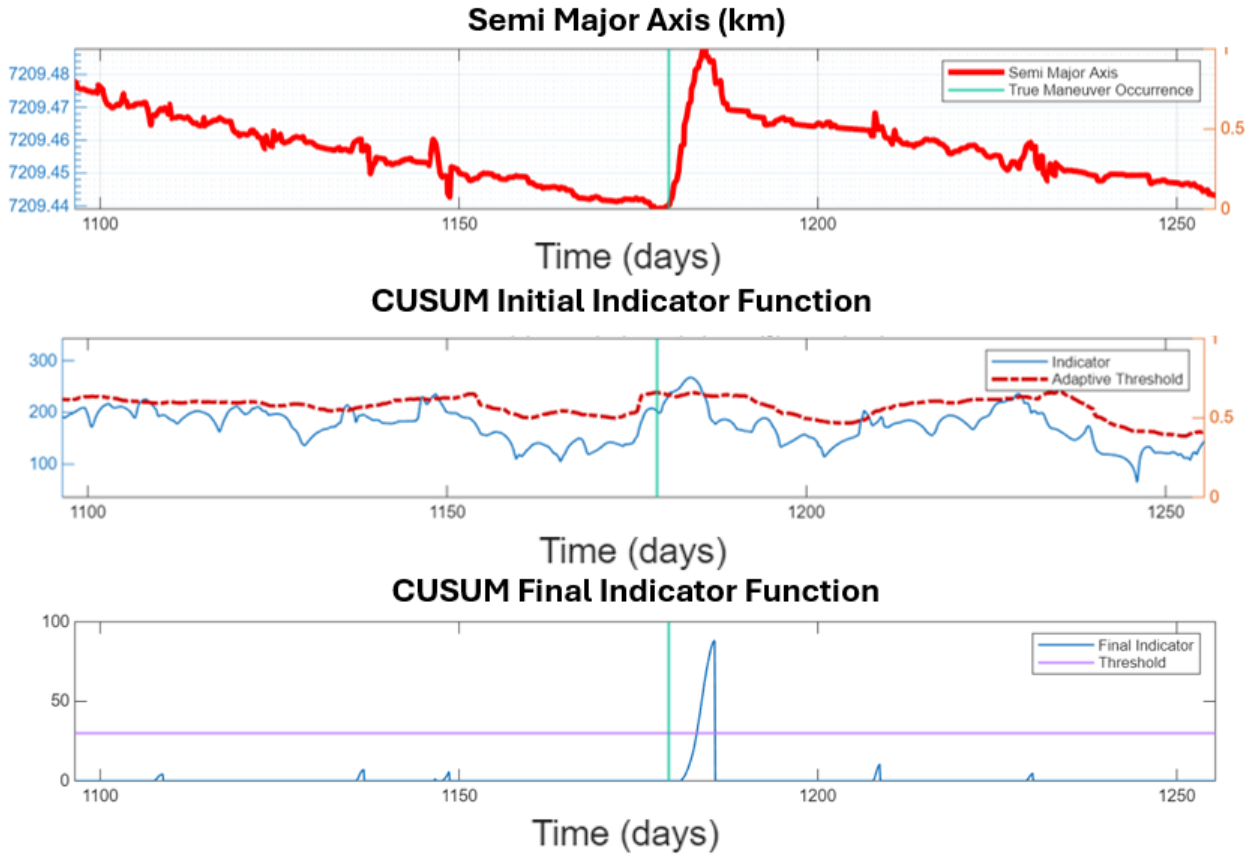

Figure 9: TLE data segment with single maneuver occurrence (top). CuSum indicator function and adaptive threshold (middle). Final indicator from graphical integration between indicator and adaptive threshold preventing false alarm from unsustained anomalies (bottom).

4. Results

The semi-major axis data from the TLE sets of the six RSOs constitutes the basis for predicting maneuver occurrences and compared to the maneuver logs to evaluate the algorithm's performance. Algorithm performance results for the aggregate of the 6 observed RSOs can be seen in Table 1. By varying the CuSum and threshold parameters a tradeoff between catch rate and false alarm rate can be seen between trials. The breakdown of the third trial for each satellite can be seen in Table 2 using the same set of adjustable parameters for all. While performance varied between RSOs, the catch rate remained above 96% and the rate of days per false alarm remained above 400 for all.

Table 1: Low Earth orbit satellite maneuver detection results.

Trial(Varied Paramters)	Catches/Maneuver	Catch Rate	Days/False Alarm
1	405/412	98.30%	284.2
2	402/412	97.57%	369.8
3	***399/412***	***96.84%***	***439.9***
4	397/412	96.36%	499.3
5	382/412	92.72%	637.0

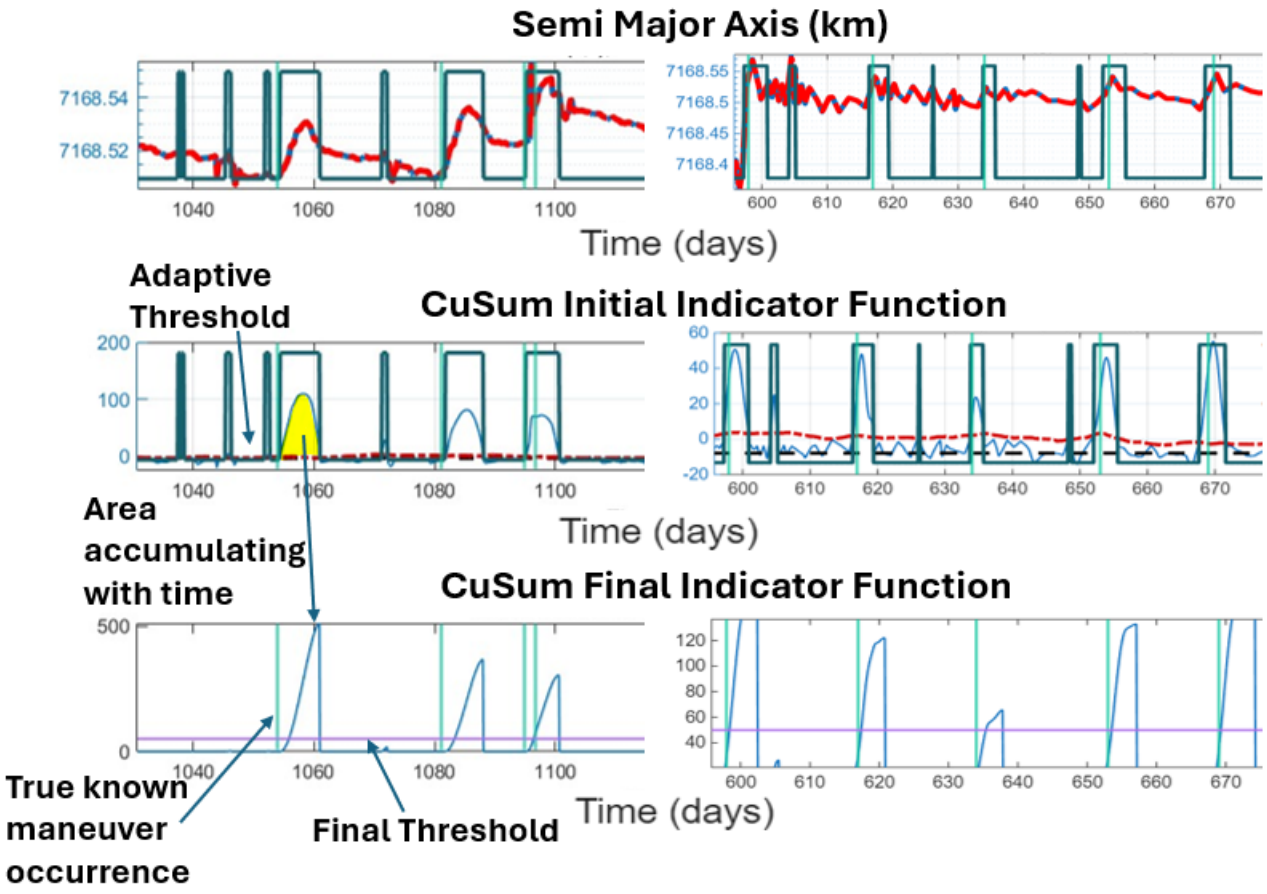

Figure 10: Algorithm successful execution on data segment with easily recognizable maneuvers (left) and more challenging data segment (right).

Table 2: Individual RSO maneuver detection results.

RSO (NORAD ID)	Catches/Maneuver	Catch Rate	Days/False Alarm
Sentinel-3A (41335)	49/51	96.08%	2210
SPOT 5 (27421)	47/49	95.92%	644
Envisat (27386)	101/104	97.12%	859
CryoSat-2 (36508)	107/111	96.40%	201
SPOT 4 (25260)	43/44	97.73%	408
SARAL (39086)	52/53	98.11%	3169
Total	399/412	96.84%	637

V. CUSUM MANEUVER DETECTION IN CISLUNAR SPACE

1. Cislunar Mission Data

To test the CuSum algorithm's effectiveness in this area, ephemerides from two cislunar missions with maneuvers out of Lissajous orbits are leveraged. These missions both include quasi-periodic cislunar phases that transition into lunar orbit, as seen in Figures 11 and 12. The algorithm's results are compared to logged maneuver times. These maneuvers include both smaller station-keeping maneuvers [22] and larger transfer maneuvers for lunar transfer insertion (LTI) and lunar orbit insertion

(LOI) [23].

As previously discussed, for cislunar systems, the Jacobi constant J is a parameter that serves as a reliable orbit invariant for maneuver detection. State data in the ephemerides as shown in equations (12) - (14) provide the Jacobi constant.

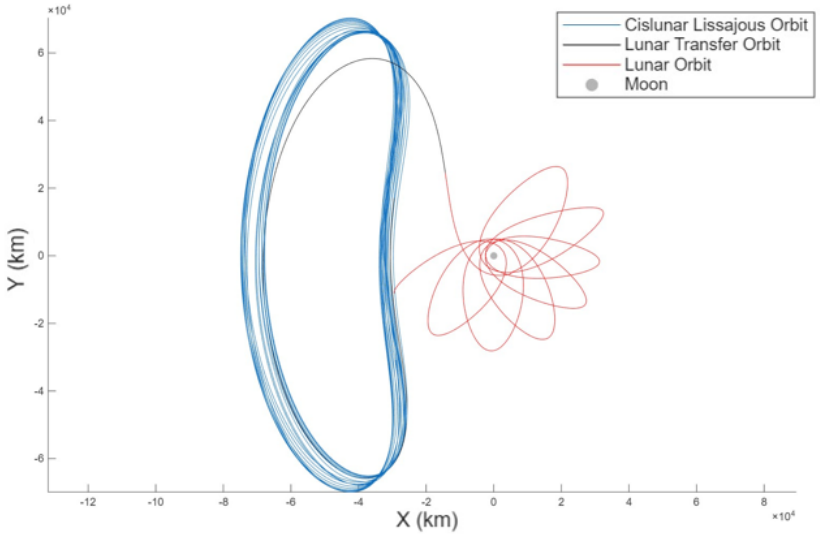

Figure 11: Artemis P2 trajectory in Earth-Moon synodic frame.

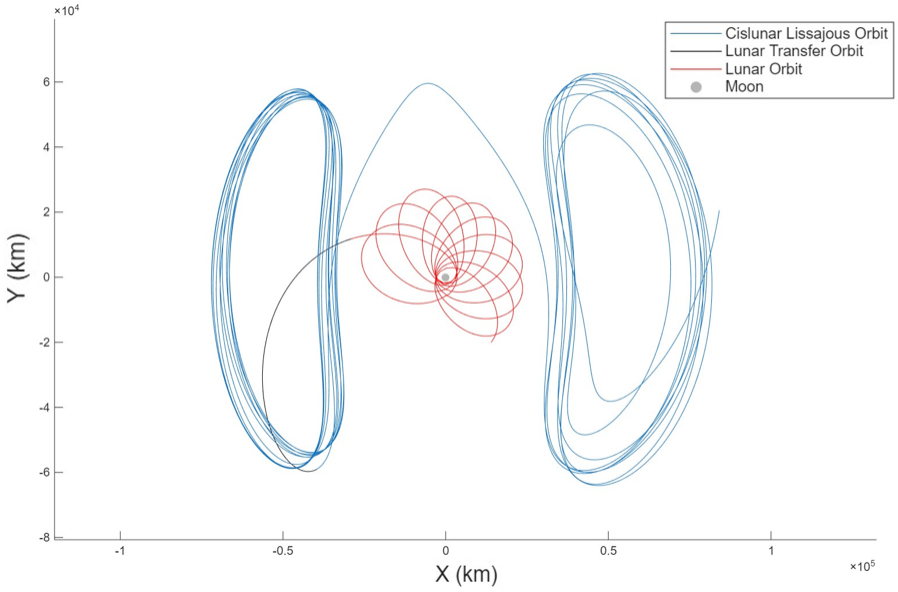

Figure 12: Artemis P1 trajectory in Earth-Moon synodic frame.

2. Application on Observed Cislunar Trajectories

Due to perturbations that separate the cislunar environment from an idealized circular restricted three body system, the Jacobi constant does not remain invariant, but experiences oscillations due to deviations from this idealized such as the non-zero eccentricity of the Moon's orbit or the exchanging of energy between the spacecraft and the moon. To mitigate the deleterious oscillatory effects of this perturbation, a high-pass filter was applied to the Jacobi constant to generate a zero-mean residual. The high-pass filter allows only for high frequency components of the signal, such as impulse maneuvers, to remain while lower frequency oscillations (those below 10^{-4} hertz), such as those caused by the nonidealized reality of cislunar dynamics, are

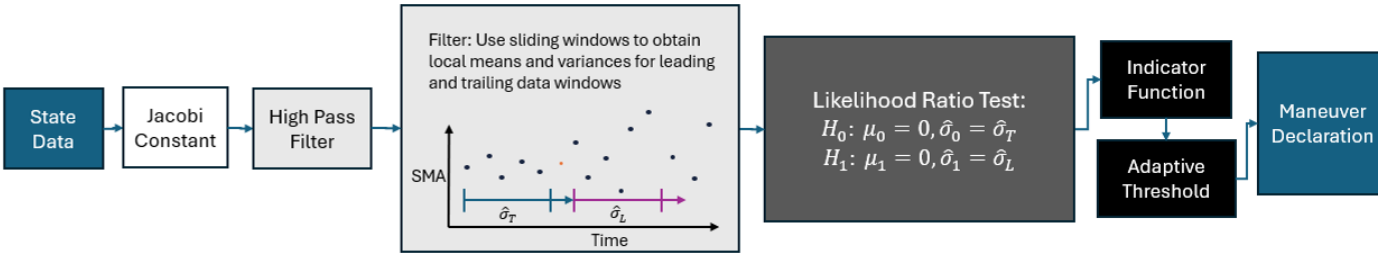

Figure 13: Cislunar maneuver detection algorithm architecture.

removed. Unlike the tracked signals used for maneuver detection of Earth-orbiting RSOs, maneuvers cause changes in variance of this residual rather than in mean as a result of the high-pass filter. Because of this, alternate hypotheses were used for the CuSum, assuming a mean of zero for both. Instead, two sliding windows estimate the signal's variance forwards and back in time. The local standard variances can be estimated using (33). The jump and null hypotheses can be seen in equations (56) and (57).

$$H_0 : \mu = 0, \sigma = \sigma_T \tag{56}$$

$$H_1 : \mu = 0, \sigma = \sigma_L \tag{57}$$

These hypotheses are implemented with the rest of the CuSum algorithm in equations (17) - (20) to find the summation term S shown in (58). This term is then used in equation (22) to generate an indicator h.

$$S\left(n\right) = \sum_{k=1}^{n} \ln \frac{\sigma_T}{\sigma_L} + \frac{(x(k))^2(\sigma_L^2 - \sigma_T^2)}{2\sigma_T^2\sigma_L^2} \tag{58}$$

The resulting indicator function can then have a threshold test applied. This threshold is made adaptive using the same approach described previously and shown in equations (34) and (35). Figure 13 illustrates the full high-pass CuSum algorithm.

3. Results

The results of this algorithm for both Artemis P1 and P2 can be seen in table 3. The algorithm successfully caught over 98% of maneuvers while maintaining a false alarm rate of less than one in every 68 days. The maneuvers for each spacecraft include two orbit transfer maneuvers and thirty station keeping ones. Further tuning of the threshold parameters can be used to increase catch rate at the expense of a higher false alarm rate or the opposite.

Table 3: Cislunar satellite maneuver detection results.

Spacecraft	Catches/Maneuver	Catch Rate	Days/False Alarm
Artemis P2	31/32	96.88%	77.33
Artemis P1	32/32	100%	62
Total	63/64	98.44%	68.57

The transfer maneuvers being large in magnitude when compared to most station-keeping maneuvers are proven to have a significant effect on the Jacobi constant making them straightforward to catch. The Jacobi constant, its filtered signal, and the resulting indicator function for these two maneuvers on Artemis P1 can be seen in Figure **??**.

Station-keeping maneuvers are typically smaller in size than orbit transfer maneuvers and inflict smaller changes on the Jacobi constant. The distribution of the sizes of these maneuvers is shown in Figure 15. However, the CuSum algorithm is still able to detect. The Jacobi constant, its filtered signal, and the resulting indicator function for the station-keeping period of Artemis P1 can be seen in Figure 16.

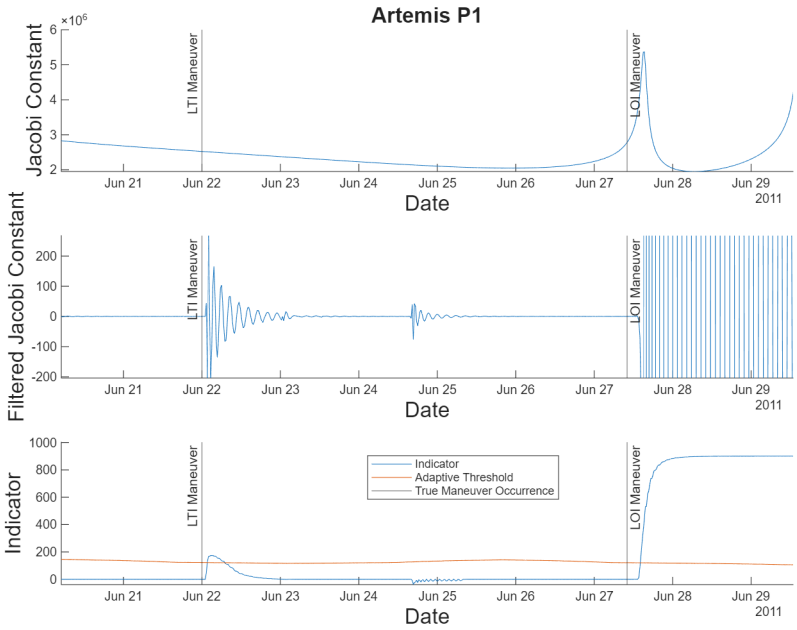

Figure 14: Artemis P1 orbit transfer maneuvers Jacobi constant data (top), high-pass filtered Jacobi constant data (middle), and resulting indicator function and adaptive threshold (bottom).

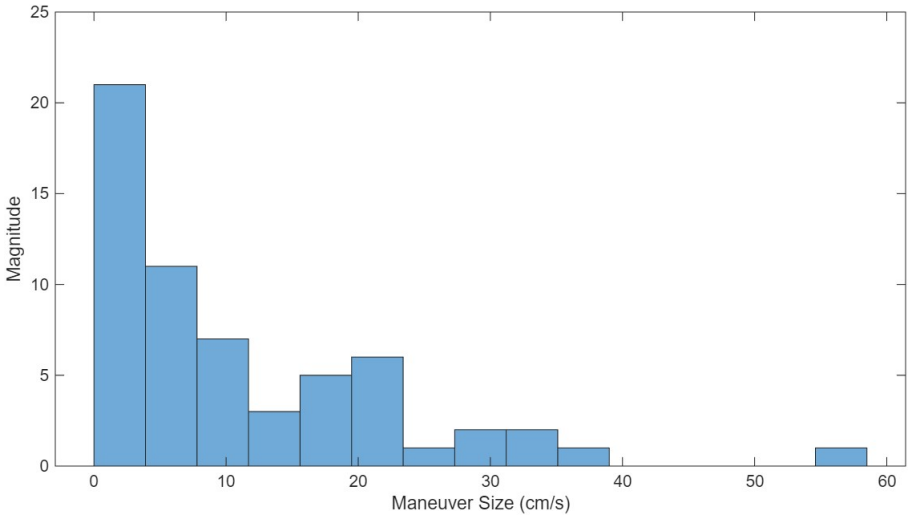

Figure 15: Cislunar station-keeping maneuver size distribution.

VI. CONCLUSIONS

Maneuver detection is a key component of RSO tracking and plays an essential role across many subjects of interest including space situational awareness and celestial navigation. This study introduces adaptive CuSum based methods that are applied to different dynamical situations. By monitoring orbital invariant signals, the CuSum based approaches are effective at recognizing maneuvers small in magnitude relative to noise and provide the capability to leverage a good model or be strictly data driven. The efficacy of the adaptive model based CuSum algorithm is demonstrated on simulated RSO trajectory data. The data-driven multiple CuSum algorithm is demonstrated on TLE data of real life RSOs and compared to known maneuver instances to validate its results of over 96% catch rates with rates of false alarms of less than one for every 400 days. The ability to automatically tune is also provided to focus on catch rate vs false alarm rate as well. Lastly, the application of real cislunar ephemeris and maneuver data verifies the high-pass CuSum algorithm developed to leverage the relative stability of the Jacobi constant term in the chaotic and more difficult to track cislunar space. This automatic algorithm is able to achieve over an 98% catch rates with false alarms occurring less than once every 68 days.

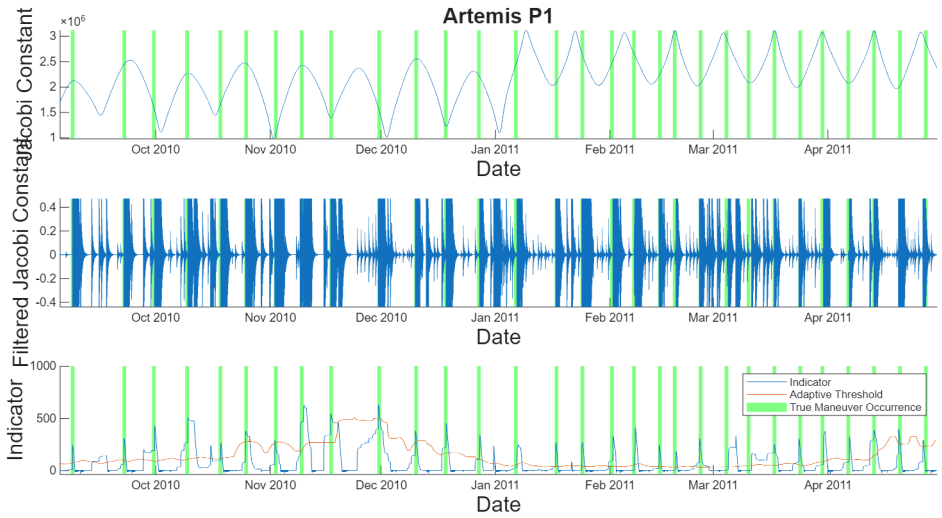

Figure 16: Artemis P1 station keeping period Jacobi constant and maneuver time data (top), high-pass filtered Jacobi constant data (middle), and resulting indicator function and adaptive threshold (bottom).

REFERENCES

[1] M. J. Holzinger et al. *A primer on cislunar space*. eng. AFRL ; 2021-1271. Wright-Patterson AFB, OH: [Air Force Research Laboratory], 2021.

[2] Stijn Lemmens and Holger Krag. "Two-Line-Elements-Based Maneuver Detection Methods for Satellites in Low Earth Orbit". In: *Journal of Guidance Control Dynamics* 37.3 (May 2014), pp. 860–868. DOI: 10.2514/1.61300.

[3] T. Kelecy et al. "Satellite Maneuver Detection Using Two-line Elements Data". In: *Advanced Maui Optical and Space Surveillance Technologies Conference*. Ed. by S. Ryan. Jan. 2007, E19, E19.

[4] Russell Patera. "Space Event Detection Method". In: *Journal of Spacecraft and Rockets - J SPACECRAFT ROCKET* 45 (May 2008), pp. 554–559. DOI: 10.2514/1.30348.

[5] Zachary Folcik, Paul Cefola, and R.I. Abbot. "Geo maneuver detection for space situational awareness". In: *Advances in the Astronautical Sciences* 129 (Jan. 2008), pp. 523–550.

[6] Alejandro Pastor et al. "Satellite maneuver detection and estimation with optical survey observations". In: *Journal of the Astronautical Sciences* 69.3 (June 2022), pp. 879–917. DOI: 10.1007/s40295-022-00311-5.

[7] Lorenzo Porcelli et al. "Satellite maneuver detection and estimation with radar survey observations". In: *Acta Astronautica* 201 (2022), pp. 274–287. ISSN: 0094-5765. DOI: 10.1016/j.actaastro.2022.08.021. URL: https://www.sciencedirect.com/science/article/pii/S0094576522004258.

[8] Nicholas Perovich, Zachary Folcik, and Rafael Jaimes. "Satellite Maneuver Detection Using Machine Learning and Neural Network Methods Behaviors". In: *2022 IEEE Aerospace Conference (AERO)*. 2022, pp. 01–19. DOI: 10.1109/AERO53065.2022.9843412.

[9] E. S. Page. "Continuous inspection schemes". In: *Biometrika* 41.1/2 (1954), pp. 100–115.

[10] K. W. Kemp. "The average run length of the cumulative sum chart when a V-mask is used". In: *Journal of the Royal Statistical Society. Series B (Methodological)* 23.1 (1961), pp. 149–153.

[11] Douglas M. Hawkins and David H. Olwell. *Cumulative sum charts and charting for quality improvement*. Springer Science & Business Media, 1998.

[12] David A. Vallado and Wayne D. McClain. *Fundamentals of astrodynamics and applications*. eng. 4th ed. Space technology library. Hawthorne, CA: Microcosm Press, 2013. ISBN: 9781881883180.

[13] Pierre Granjon. "The CuSum algorithm - a small review". In: (June 2013).

[14] M. Basseville and A. Benveniste. *Detection of Abrupt Changes in Signals and Dynamical Systems*. Springer Berlin, Heidelberg, 1986.

[15] Meysam Mahooti. *High Precision Orbit Propagator*. 2026. URL: https://www.mathworks.com/matlabcentral/fileexchange/55167-high-precision-orbit-propagator.

[16] M.-A. Massoumnia, G.C. Verghese, and A.S. Willsky. "Failure detection and identification". In: *IEEE Transactions on Automatic Control* 34.3 (1989), pp. 316–321. DOI: 10.1109/9.16422.

[17] Michèle Basseville and Igor Nikiforov. *Detection of Abrupt Change Theory and Application*. Vol. 15. Apr. 1993. ISBN: 0-13-126780-9.

[18] R. Mangoubi. *Robust Estimation and Failure Detection*. Wright-Patterson AFB, OH: Springer London, 1998.

[19] Ramses M. Agustin et al. “Robust Failure Detection for Reentry Vehicle Attitude Control Systems”. In: *Journal of Guidance, Control, and Dynamics* 22.6 (1999), pp. 839–845. DOI: 10.2514/2.4461. eprint: https://doi.org/10.2514/2.4461. URL: https://doi.org/10.2514/2.4461.
[20] *Space-track.org*. URL: https://www.space-track.org/.
[21] *Space segment*. URL: https://ids-doris.org/resources/technical-documents.html.
[22] David Folta, Mark Woodard, and Daniel Cosgrove. “Stationkeeping of the First Earth-Moon Libration Orbiters - The ARTEMIS Mission”. In: *Advances in the Astronautical Sciences* 142 (Jan. 2011).
[23] Theodore H. Sweetser et al. “ARTEMIS Mission Design”. In: 165.1-4 (Dec. 2011), pp. 27–57. DOI: 10.1007/s11214-012-9869-1.

ACKNOWLEDGEMENTS

The authors would like to thank Greg Blasche, Stephanie Golmon, and David Baumgart for supporting the early stages of this work as well as Scott Dellicker, Chris McDowell, and Neil Hallock for supporting its continuation.

This version was uploaded on 06-23-2026 and supersedes the previous release on 06-04-2026